VELOCITY DETERMINATION BY IMAGE-WAVE REMIGRATION

A. Novais, J. Costa, and J. Schleicher

email: *amelia@ime.unicamp.br*
keywords: *velocity continuation, migration*

ABSTRACT

We have implemented a finite-difference algorithm for image-wave time-remigration in FORTRAN 90, and studied its theoretical properties in detail. For a number of synthetic models, numerical experiments have been realized. For these examples, we obtained perfect agreement between the theoretical predictions and numerical results. The examples also prove the computational efficiency of the algorithm. An example using ground-penetrating-radar (GPR) data demonstrates how image-wave remigration can be used to estimate a model of the medium velocity.

INTRODUCTION

The objective of seismic migration is the construction of an image of the geological structure of the underground using recordings of seismic waves that have propagated through this medium. An update of the migrated image, which might turn out to be necessary, for example, if the image was obtained using an incorrect velocity model and an improved model has become available, is often referred to as remigration.

To construct a subsurface image from time sections, it is necessary to carry out a migration. This process repositions the reflectors and collapses the diffractions, in this way generating an image that actually represents the geometry of the reflecting interfaces in the underground. For a successful application of a seismic migration, the knowledge of the velocity distribution in the underground is essential. In this work, we demonstrate the implementation of a strategy to construct a set of migrated images in a very fast way, each for a different velocity value. The permitted values for the migration velocity can vary in a user-defined range. The result of this process is a sequence of images that can be evaluated by the interpreter. In this way, he can choose that particular image and migration velocity which best satisfies his given interpretive criteria.

The necessity to improve a given migrated image is frequent in seismic and ground-penetrating-radar (GPR) applications. The reason is that the correct velocity model is unknown and has to be determined during the process of constructing the best possible image. In conventional seismic processing, the estimation of a velocity model is carried out by constructing velocity panels from CMP gathers using different offsets. However, this is not a common procedure in GPR processing.

This work is based on the velocity-continuation procedure as originally proposed by Fomel (1994) (see also Hubral et al., 1996; Fomel, 2003a,b). We have implemented a finite-difference algorithm in FORTRAN 90, and studied its theoretical properties in detail. For a number of synthetic models, numerical experiments have been realized. For these examples, we obtained perfect agreement between the theoretical predictions and numerical results. The examples also prove the computational efficiency of the algorithm.

As a more practical test, the method has also been applied to real GPR data. By picking local velocities from the remigrated panels, it was possible to determine a laterally varying velocity model that could be successfully used for a subsequent time migration of the data.

CONTINUATION EQUATION

In this section, we present the method of velocity continuation for seismic zero-offset data in a medium with constant velocity. All our theoretical results and numerical algorithms can be directly applied to GPR data.

When ignoring amplitude effects, the process of velocity continuation for zero-offset data can be described by the partial differential equation (Fomel, 1994; Hubral et al., 1996; Fomel, 2003a,b; Claerbout, 1986)

$$\frac{\partial^2 P}{\partial v \partial t} + vt\frac{\partial^2 P}{\partial x^2} = 0, \tag{1}$$

where $P = P(x, t, v)$ is the zero-offset section that is to be remigrated in velocity v, t is the vertical time and x is the coordinate of the source-receiver pair. Each section of constant velocity v corresponds to one image. To solve equation (1), we need an initial and a boundary condition. The initial condition is given by the original migrated image, $P_0(x, t)$. The boundary condition can be taken from the condition that outside the migrated range, no image will be obtained. Then, the conditions read

$$P|_{t=T} = 0 \quad P|_{v=v_0} = P_0(x, t), \tag{2}$$

where v_0 is the initial velocity, and T is the boundary time. We need to choose $T = 0$ for continuations to smaller velocities and $T = t_{\text{max}}$, i.e., the largest time value of the image, for a continuation to greater velocities.

FINITE-DIFFERENCE APPROXIMATION

We use the finite-difference method to solve the problem given by equations (1)–(2). We discretize the variables in the following way: $x_l = x_0 + l\Delta x$, $t_m = t_0 + m\Delta t$ e $v_n = v_0 + n\Delta v$, where x_0, t_0 and v_0 are the initial midpoint, time, and velocity value, respectively. We denote the pressure field $P(x_l, t_m, v_n)$ by $P^n_{l,m}$. We discretize the equation at the point $(x_l, t_{m+1/2}, v_{n+1/2})$, using a centered scheme for both first derivatives in the mixed-derivative term and a second-order centered scheme for the second derivative with respect to x. In this way, we have for the mixed derivative

$$\left.\frac{\partial^2 P}{\partial v \partial t}\right|_{l,m+\frac{1}{2},n+\frac{1}{2}} = \frac{P^{n+1}_{l,m+1} - P^{n+1}_{l,m} - P^n_{l,m+1} + P^n_{l,m}}{\Delta v \Delta t}. \tag{3}$$

To discretize the second term of equation (1), we use the mean value of the operator in the vertices, as indicated in Figure 1 (Fomel, 2003a). In this way, we obtain

$$vt\left.\frac{\partial^2 P}{\partial x^2}\right|_{l,m+\frac{1}{2},n+\frac{1}{2}} = \frac{1}{4}\left(v_n t_m \mathbf{D}_x P^n_{l,m} + v_{n+1} t_m \mathbf{D}_x P^{n+1}_{l,m} + v_n t_{m+1} \mathbf{D}_x P^n_{l,m+1} + v_{n+1} t_{m+1} \mathbf{D}_x P^{n+1}_{l,m+1}\right), \tag{4}$$

with $\mathbf{D}_x$ being the second-order centered finite-difference operator for the second derivative with respect to x, i.e.,

$$\mathbf{D}_x P^n_{l,m} = \frac{P^n_{l+1,m} - 2P^n_{l,m} + P^n_{l-1,m}}{\Delta x^2}. \tag{5}$$

Substituting the approximations (3) and (4) in equation (1), we obtain two inconditionally stable FD schemes. The first one is forward in velocity and backward in time,

$$(1 - a^{n+1}_m \mathbf{D}_x) P^{n+1}_{l,m} = (1 + a^{n+1}_{m+1} \mathbf{D}_x) P^{n+1}_{l,m+1} - (1 - a^n_{m+1} \mathbf{D}_x) P^n_{l,m+1} + (1 + a^n_m \mathbf{D}_x) P^n_{l,m}, \tag{6}$$

where $a^n_m = (v_n t_m \Delta v \Delta t)/4$. The second scheme is forward in time and backward in velocity,

$$(1 - a^n_{m+1} \mathbf{D}_x) P^n_{l,m+1} = (1 + a^{n+1}_{m+1} \mathbf{D}_x) P^{n+1}_{l,m+1} - (1 - a^{n+1}_m \mathbf{D}_x) P^{n+1}_{l,m} + (1 + a^n_m \mathbf{D}_x) P^n_{l,m}, \tag{7}$$

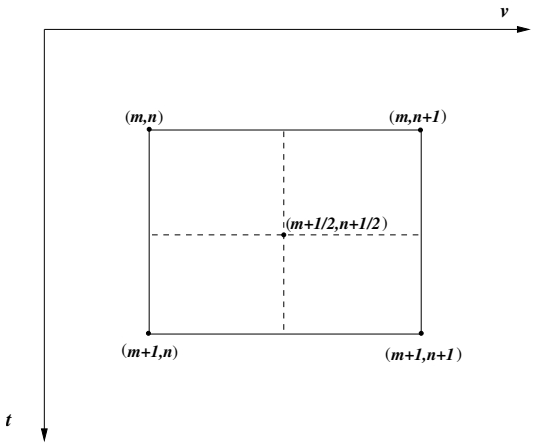

Figure 1: Discretization of the second derivative at point $(x_l, t_{m+1/2}, v_{n+1/2})$.

with the same a_m^n. Scheme (6) is inconditionally stable for increasing velocity and decreasing time, while scheme (7) is inconditionally stable for decreasing velocity and increasing time.

In this work, we have implemented scheme (6), which is more convenient to describe a practical time remigration, since a zero-offset section can be thought of as a time-migrated section with zero migration velocity.

Numerical stability

To analyze the numerical stability of scheme (6), we utilize the von Neumann criterion (Strikwerda, 1989; Thomas, 1995). For that purpose, we substitute $P_{l,m}^n = \xi^n \exp(i\,(l\theta_x + m\theta_t))$ in scheme (6) to obtain

$$(\xi - 1)\left(e^{i\,\theta_t} - 1\right) = b_m^n + \xi b_m^{n+1} + b_{m+1}^n e^{i\,\theta_t} + \xi b_{m+1}^{n+1} e^{i\,\theta_t}\,, \tag{8}$$

where

$$\begin{aligned} b_m^n &= a_m^n\,\frac{4\sin^2(\theta_x/2)}{\Delta x^2} \\ &= v_n t_m\,\frac{\Delta v \Delta t}{\Delta x^2}\,\sin^2(\theta_x/2) \\ &= v_n t_m \gamma\,. \end{aligned} \tag{9}$$

Equation (8) can be solved for ξ to yield

$$\xi = \frac{e^{i\,\theta_t} - 1 + \gamma v_n (t_m + t_{m+1} e^{i\,\theta_t})}{e^{i\,\theta_t} - 1 - \gamma v_{n+1}(t_m + t_{m+1} e^{i\,\theta_t})}\,. \tag{10}$$

After some algebric operations, this can be written as

$$\xi = \frac{2 - \gamma v_n\left[t_m - t_{m+1} + i(t_m + t_{m+1})\cot(\theta_t/2)\right]}{2 + \gamma v_{n+1}\left[t_m - t_{m+1} + i(t_m + t_{m+1})\cot(\theta_t/2)\right]}\,. \tag{11}$$

From this expression for ξ, we can immediately conclude that for $v_{n+1} > v_n$ and $t_{m+1} < t_m$,

$$|\xi|^2 = \frac{\left[2 - \gamma v_n (t_m - t_{m+1})\right]^2 + \left[\gamma v_n (t_m + t_{m+1})\cot(\theta_t/2)\right]^2}{\left[2 + \gamma v_{n+1}(t_m - t_{m+1})\right]^2 + \left[\gamma v_{n+1}(t_m + t_{m+1})\cot(\theta_t/2)\right]^2} \leq 1\,. \tag{12}$$

As a consequence, when considering increasing velocity and decreasing time, this FD scheme is inconditionally stable for any grid spacing

To prove that scheme (7) is inconditionally stable, too, it is sufficient to apply the same procedure that was used above. We conclude that the latter scheme is inconditionally stable for decreasing velocities and increasing time.

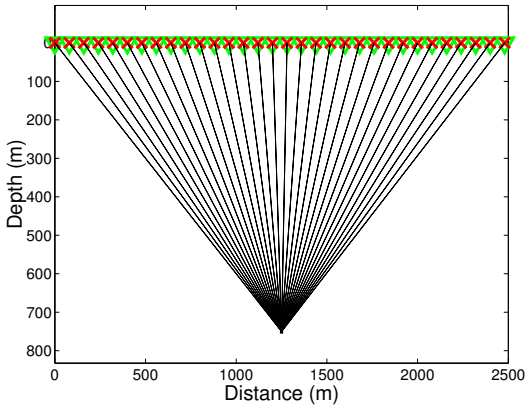

Figure 2: Model 1: Constant-velocity medium with a single diffraction point.

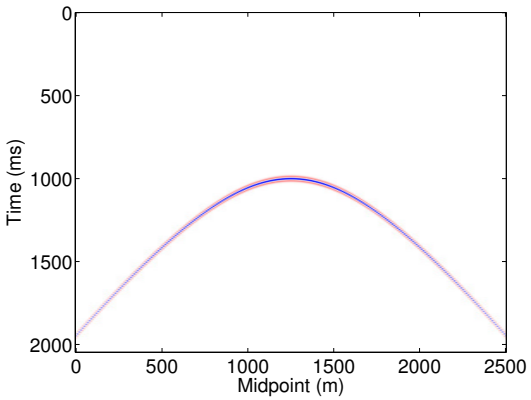

Figure 3: Zero-offset section, which corresponds to a time-migrated section with velocity 0 m/s.

NUMERICAL EXPERIMENTS

As a next step, we tested the implementation with several synthetic data sets. Of these, we discuss here one model with a single diffraction point and one with a syncline reflector. Finally, we applied the method to a real GPR data set.

Diffractor model

The first model consists of a diffraction point in a horizontal position at $x = 1250$ m and depth $z = 750$ m. It is depicted in Figure 2 together with the corresponding ray family. The corresponding zero-offset section was modeled with a Ricker source pulse with a dominant frequency of 31.25 Hz. The true propagation medium has a velocity of 1500 m/s (i.e., water velocity). For the zero-offset simulation, 200 source-receiver pairs were distributed along the surface symmetrically around the diffraction point, regularly space at a distance of 10 m. The sampling rate was 2 ms. Therefore, in the finite-difference computations, $\Delta x = 10$ m and $\Delta t = 2$ ms.

Figure 3 shows the modeled zero-offset section that corresponds to a time-migrated section with a velocity of 0 m/s. Figures 4a-f depict several remigrated sections for different values of the migration velocity. We can clearly observe the collaps of the diffraction when the migration velocity becomes close to the true medium velocity of 1500 m/s. Beyond this velocity, the diffraction event starts to change its shape, so that the concavity, which originally was downward, now becomes upward. For velocities greater than the true medium velocity, all migrated images have this appearance.

Synclinal model

Our second test with synthetic data is to apply the image-wave velocity continuation to a model where the wavefield has passed to a caustic. The second model can be seen in Figure 5. The zero-offset section is depicted in Figure 6, where the CMP spacing was chosen as 10 m. The source pulse was again a Ricker wavelet, now with a dominant frequency of 31.25 Hz. The true velocity of the propagation medium is 3000 m/s, in which two reflecting interfaces are embedded. The zero-offset section was simulated using the exploding-reflector model (Loewenthal et al., 1976). Since the second reflector is a synclinal structure, the zero-offset section presents the well-known bow-tie structure.

The snapshots of the image-wave propagation are shown in Figure 7. We see that as the velocity increases, the bow tie unfolds. In the section for velocity 2800 m/s, Figure 7c, the bow tie has already disappeared. From that velocity on, the reflector starts to smooth out. At the velocity of 3000 m/s, it has arrived at its correct shape. As the velocity continues to increase, the synclinal structure is becoming broader and broader.

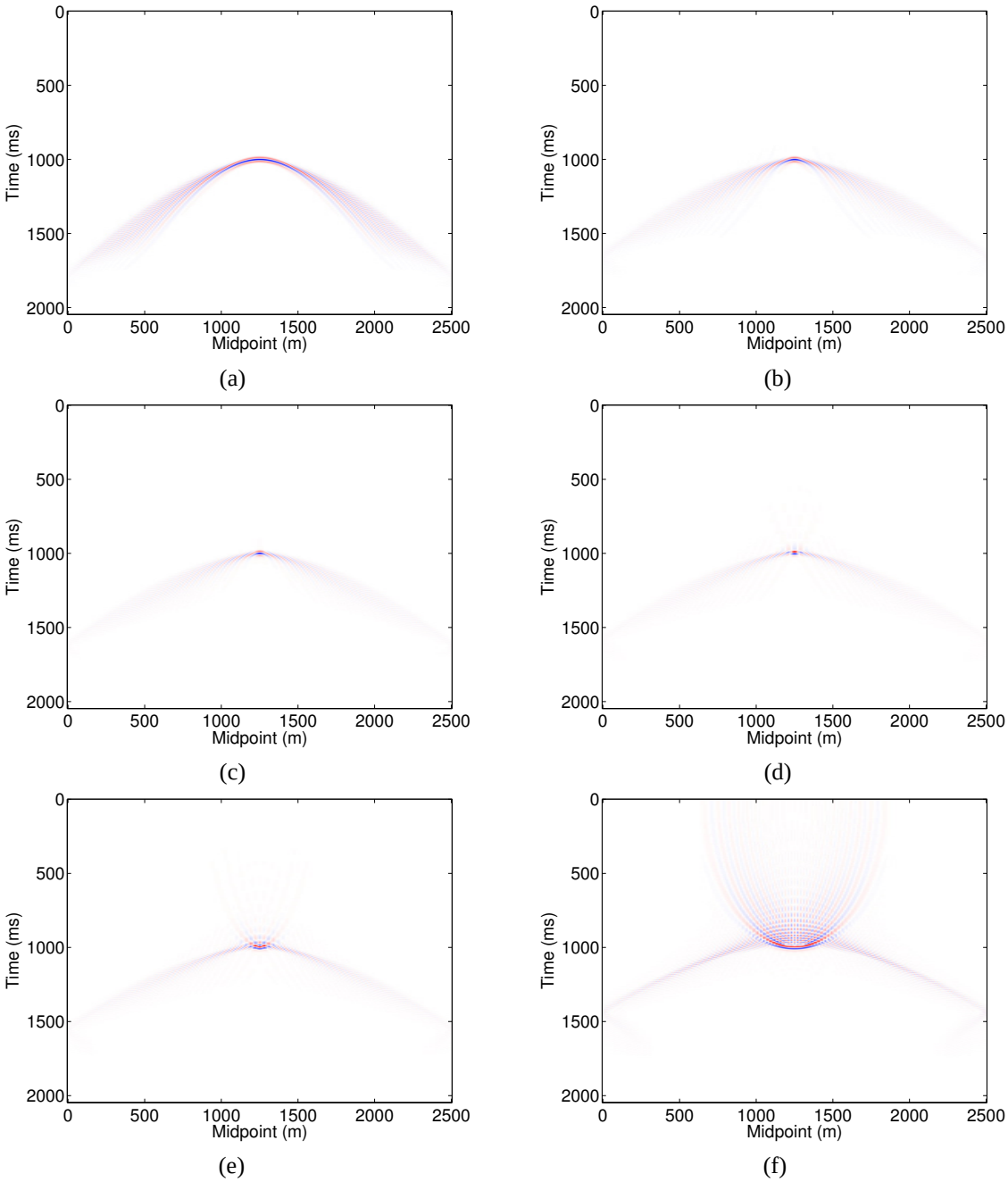

Figure 4: Remigration of synthetic diffraction data. Velocity is: (a) 1000 m/s; (b) 1400 m/s; (c) 1500 m/s; (d) 1600 m/s; (e) 1700 m/s; and (f) 2000 m/s.

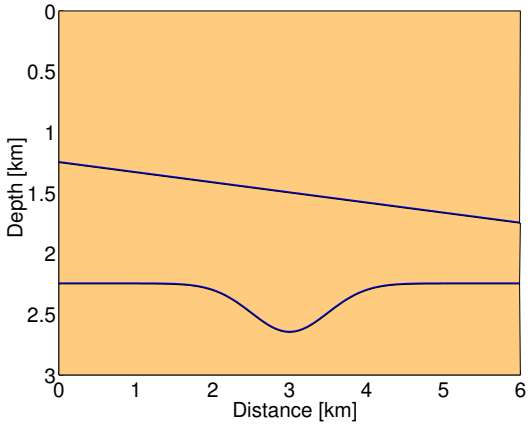

Figure 5: Model 2: Constant-velocity medium with two interfaces.

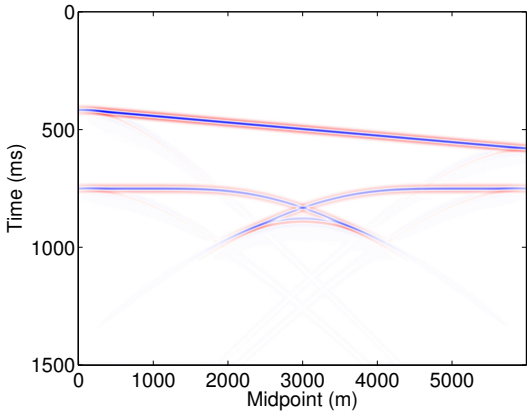

Figure 6: Zero-offset section.

From the sequence of remigrated images in Figure 7, we see that it is even possible to roughly estimate the migration velocity. Even if we did not know the true medium velocity, we could actually recognize that it must be between 2800 m/s and 3200 m/s. The reason is that only at the former velocity, the bow-tie structure unfolds and already at the latter one, the bottom of the syncline is imaged with a much smaller amplitude than the rest of the interface.

Real GPR data

As a more practical test, the method has also been applied to the real GPR data shown in Figure 8. These data were recorded at a test site of the University of São Paulo (USP) using a shielded 250 MHz antenna, a receiver spacing of 5 cm, and a sampling rate of 0.358 ns. Although the data were actually acquired with a small offset between the antennas (40 cm), the data were treated as zero-offset data. Note that the continuous, almost horizontal event across the section is the direct air wave together with the surface reflection. This event is normally removed by preprocessing. Here we are using raw data. The visible diffractions originate from seven barrels with a radius of 0.45 cm and a metallic tube with a radius of 1.9 cm. Although the subsurface geology at this site is in principle known, this knowledge has not been made use of in this test.

In Figure 9a, all diffractions are still undermigrated. Figures 9b-e show remigrated panels at velocity values where some of the diffractions focus. In Figure 9f, all diffractions are overmigrated. From this focussing features, local velocities were determined at several locations in the model by attributing the velocity values of the corresponding panels to the locations where the focussing occurs. For example, in Figure 9b the diffractions at $t = 21$ ns and $x = 28$ cm and at $t = 28.5$ ns and $x = 18$ cm focus. So, the velocity value of 5.2 cm/ns is attributed to the points $(t, x) = (21, 28)$ and $(t, x) = (28.5, 18)$. In the same way, as the diffraction at point (22.5,7) focusses in Figure 9c, we have attributed $v = 6.2$ cm/ns to this point. From the remaining panels, we have correspondingly $v = 7.0$ ns/cm at (46,14) and $v = 7.4$ cm/ns at (31,10) and (42.5,22). Moreover, we have attributed a constant velocity of 5.0 cm/ns to the near surface layer above the first diffraction.

As the next step, these local velocity picks have been used to construct a smooth velocity model by B-spline interpolation. Besides fitting the sampled values in the least squares sense, minimum gradient and curvature constraints were applied in order to obtain a unique interpolation. The resulting velocity model is depicted in Figure 10. Note that the relatively high velocities at the bottom of the model are not real but an artifact of the interpolation, which arises because there are no interpretable events below approximately 50 ns.

As a final test of its quality, the GPR data have been time migrated using the so-obtained velocity model. For this purpose, we used a hybrid migration method as introduced by Ristow and Rühl (1994), named "Fourier finite-difference migration". In this migration method, the full downward-continuation operator is

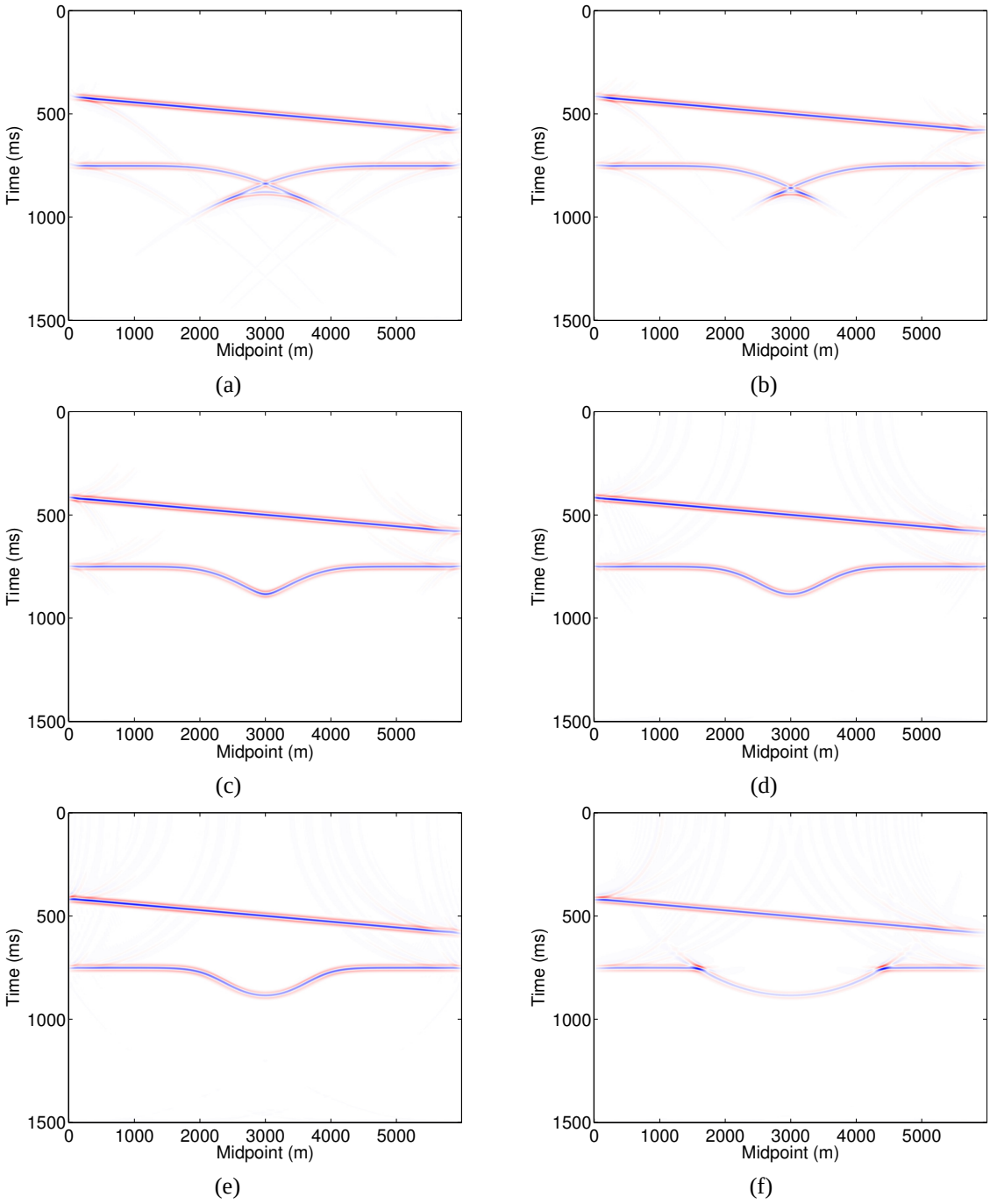

Figure 7: Remigration of synclinal structure. Velocity is: (a) 1000 m/s; (b) 2000 m/s; (c) 2800 m/s; (d) 3000 m/s; (e) 3200 m/s; and (f) 4000 m/s.

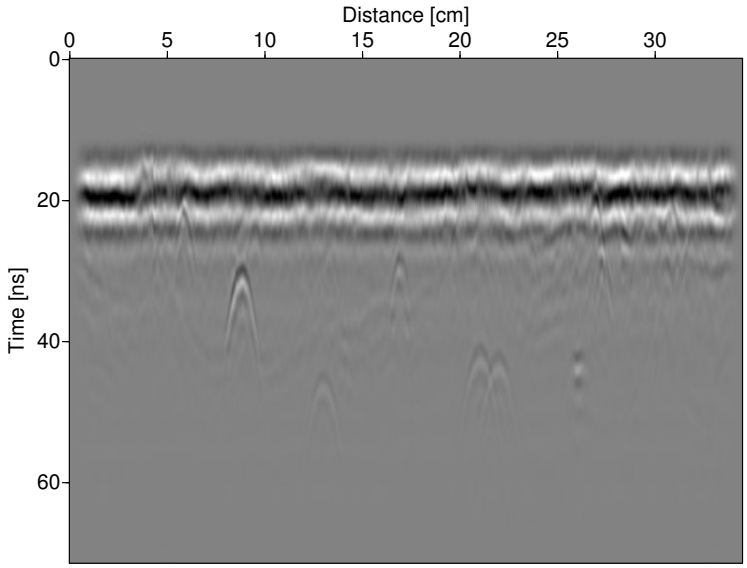

Figure 8: Real GPR data from USP test site.

split into two separate partial downward-continuation operators. The first of these partial operators realizes a phase shift of the data for a chosen constant background velocity, and the second one is an optimized finite-difference operator, taking into account the varying component of the velocity function.

The resulting time migrated image is shown in Figure 11. All diffraction are nicely focussed and the reflecting elements have a good continuity. This demonstrates that the obtained smooth velocity model is of good quality. Actually, it has been independently confirmed that the determined velocities, except for the artificial velocities at the bottom of the model, are within the range of known velocities at the known test site. We also see from Figure 11 that these artificial velocities do not affect the quality of the final migrated image. The reason is that they only occur where no interpretable events are present in the data.

CONCLUSIONS

We have shown the implementation of velocity continuation for time remigration using the finite-difference method. Through our numerical tests, we can conclude that the chosen algorithm allows to efficiently generate several migrated sections for different migration velocities. Under favorable conditions, an estimate of the best velocity can be realized by the interpreter based on the following criteria:

- If there is a diffraction event in the data, as is the case during the detection of enterred ducts, the true velocity can be determined, since at this velocity the diffraction event collapses into a single point, and for larger velocities, the concavity of the event changes.

- If there is a triplication of a reflection event in the data, these can also be employed to estimage the correct medium velocity. At the true medium velocity, the triplication unfolds and the energy is well-distributed along the event.

- For anticlinal interfaces, an upper estimate of the true medium velocity can be found from the same criterion of the distribution of the energy along the event.

The above conclusions from the test using synthetic data have been confirmed by an application of the method to real GPR data. By picking local velocities from the remigrated panels, it was possible to determine a laterally varying velocity model that could be successfully used for a subsequent time migration of the data.

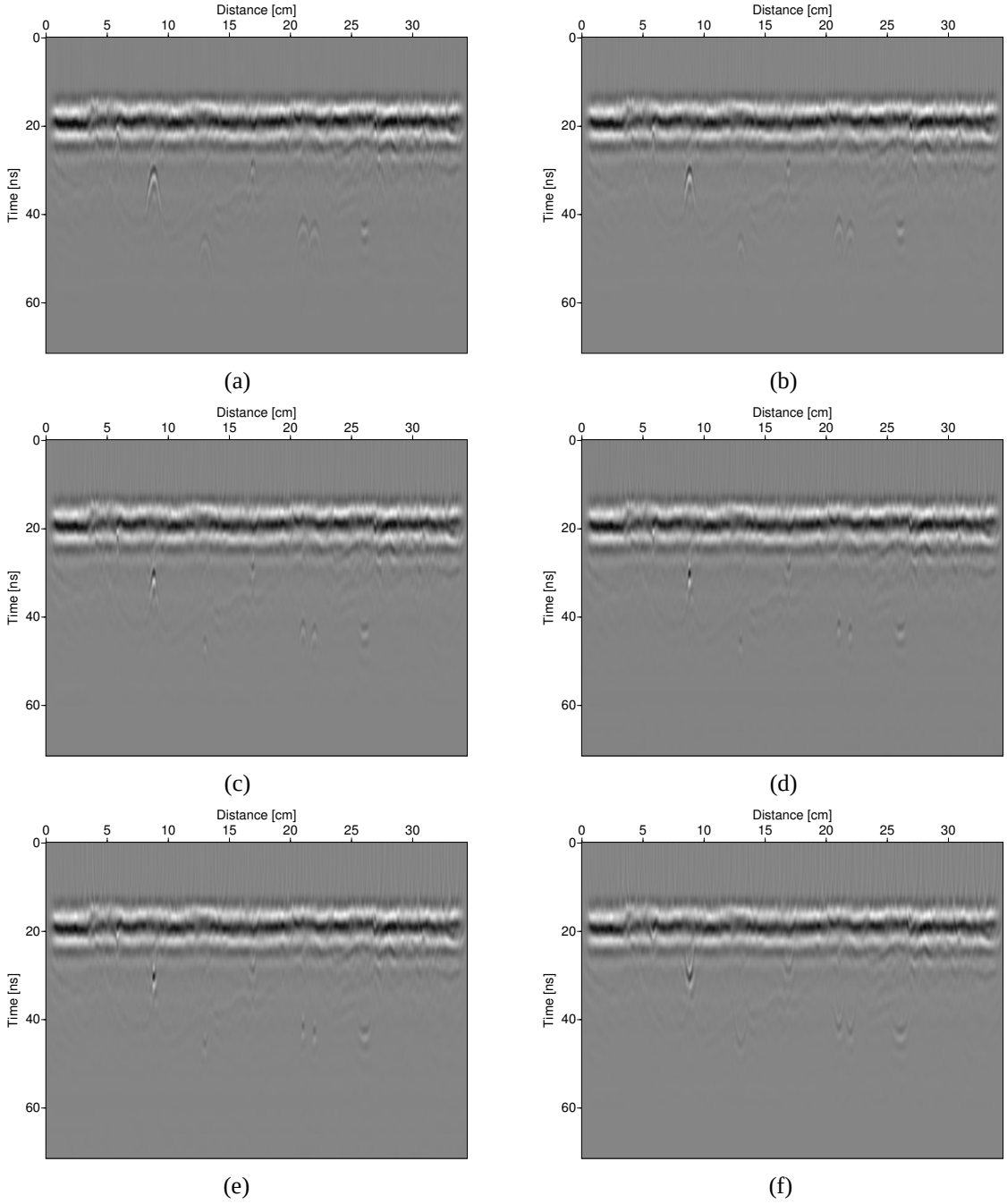

Figure 9: Remigration of real GPR data. Velocity is: (a) 4.0 cm/ns; (b) 5.2 cm/ns; (c) 6.2 cm/ns; (d) 7.0 cm/ns; (e) 7.4 cm/ns; and (f) 8.6 cm/ns.

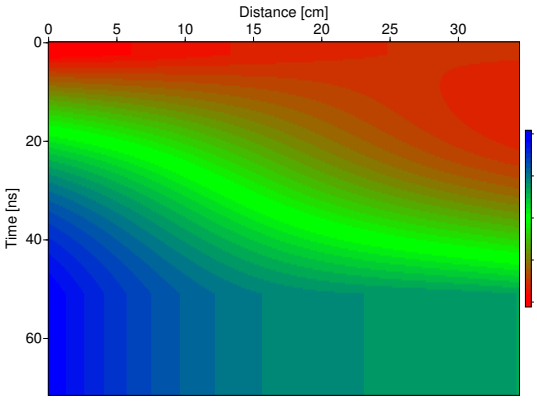

Figure 10: Velocity model as obtained from image-wave remigration after interpolation.

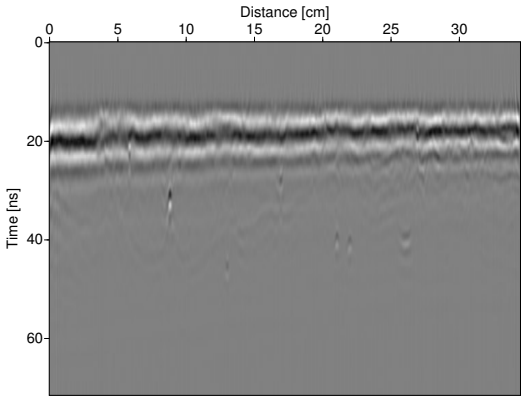

Figure 11: Migrated image of the GPR data using the velocity model of Figure 10.

ACKNOWLEDGMENTS

We are grateful to Welitom Rodrigues Borges for making the real GPR data available to us. The data were visualized with Seismic Un*x. We thank Lucas B. Freitas for his adaption of suxmovie to simplify the velocity picking. Moreover, we thank the Brazilian research agencies FAPESP and CNPq, as well as BRAIN Technologies and the sponsors of the WIT Consortium, for their financial support.

REFERENCES

Claerbout, J. F. (1986). Velocity extrapolation by cascaded 15 degree migration. Stanford Exploration Project, SEP.

Fomel, S. (1994). Method of velocity continuation in the problem of seismic. *Russian Geology and Geophysics*, 35(5):100–111.

Fomel, S. (2003a). Time migration velocity analysis by velocity continuation. *Geophysics*, 68:1662–1672.

Fomel, S. (2003b). Velocity continuation and the anatomy of residual prestack time migration. *Geophysics*, 68:1650–1661.

Hubral, P., Tygel, M., and Schleicher, J. (1996). Seismic image waves. *Geophysical Journal International*, 125:431–442.

Loewenthal, D., Lu, L., Roberson, R., and Sherwood, J. (1976). The wave equation applied to migration. *Geophysical Prospecting in press*, 24:380–399.

Ristow, D. and Rühl, T. (1994). Fourier finite-difference migration. *Geophysics*, 59(12):1882–1893.

Strikwerda, J. (1989). *Finite Difference Schemes and Partial Differential Equations*. Wadsworth & Brooks, California.

Thomas, J. (1995). *Numerical Partial Differential Equations*. Springer-Verlag, New York.